

---

# Hybrid Neural Autoencoders for Stimulus Encoding in Visual and Other Sensory Neuroprostheses

---

Anonymous Author(s)

Affiliation

Address

email

## Abstract

Sensory neuroprostheses are emerging as a promising technology to restore lost sensory function or augment human capabilities. However, sensations elicited by current devices often appear artificial and distorted. Although current models can predict the neural or perceptual response to an electrical stimulus, an optimal stimulation strategy solves the inverse problem: what is the required stimulus to produce a desired response? Here we frame this as an end-to-end optimization problem, where a deep neural network encoder is trained to invert a known, fixed forward model that approximates the underlying biological system. As a proof of concept, we demonstrate the effectiveness of our hybrid neural autoencoder (HNA) on the use case of visual neuroprostheses. We found that HNA is able to produce high-fidelity stimuli from the MNIST and COCO datasets that outperform conventional encoding strategies and surrogate techniques across all tested conditions. Overall this is an important step towards the long-standing challenge of restoring high-quality vision to people living with incurable blindness and may prove a promising solution for a variety of neuroprosthetic technologies.

## 1 Introduction

Sensory neuroprostheses are emerging as a promising technology to restore lost sensory function or augment human capacities [1, 2]. In such devices, diminished sensory modalities (e.g., hearing [3], vision [4, 5], cutaneous touch [6]) are re-enacted through streams of artificial input to the nervous system. For example, visual neuroprostheses electrically stimulate neurons in the early visual system to elicit neuronal responses that the brain interprets as visual percepts. Such devices have the potential to restore a rudimentary form of vision to millions of people living with incurable blindness.

However, all of these technologies face the challenge of interfacing with a highly nonlinear system of biological neurons whose role in perception is not fully understood. Due to the limited resolution of electrical stimulation, prostheses often create neural response patterns foreign to the brain. Consequently, sensations elicited by current sensory neuroprostheses often appear artificial and distorted [7, 8]. A major outstanding challenge is thus to identify a stimulus encoding that leads to perceptually intelligible sensations. Often there exists a numeric or symbolic forward model,  $f$  (Fig. 1A), constrained by empirical data, that can predict a neuronal or (ideally) perceptual response to the applied stimulus (see [9] for a recent review). To find the stimulus that will elicit a desired response, one essentially needs to find the inverse of the forward model,  $f^{-1}$ . However, realistic forward models are rarely analytically invertible, making this a challenging open problem for neuroprostheses.

Here we propose to approach this as an end-to-end optimization problem, where a deep neural network (DNN) (*encoder*) is trained to invert a known, fixed forward model (*decoder*, Fig. 1B). The encoder is trained to predict the patterns of electrical stimulation patterns that elicit perception (e.g., vision, audition) or neural responses (e.g., firing rates) closest to the target. This hybrid neural

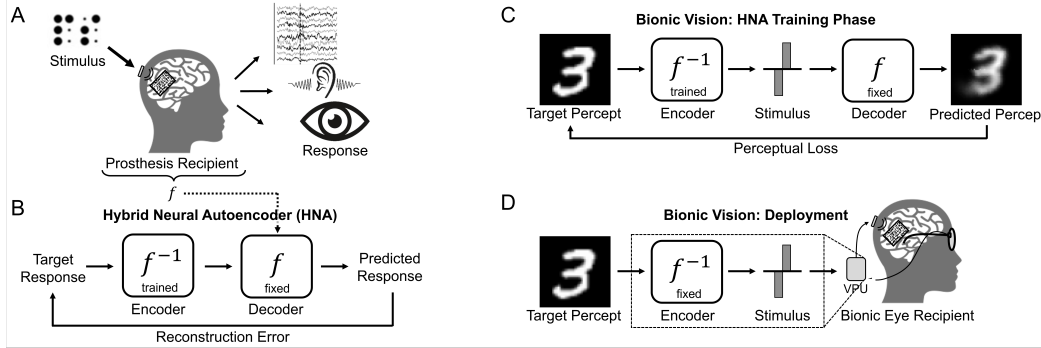


Figure 1: A) Sensory neuroprosthesis. A numeric or symbolic forward model ( $f$ ) is used to approximate the neuronal or, ideally, perceptual response to electrical stimuli. B) Hybrid neural autoencoder (HNA). A deep neural encoder ( $f^{-1}$ ) is trained to predict the patterns of electrical stimulation that elicit responses closest to the target. C) Visual neuroprostheses are one prominent application of HNA, where an encoder can be trained to predict the electrical stimulation needed to elicit a desired visual percept. D) The trained encoder is deployed on a vision processing unit (VPU), predicting stimuli in real-time that are decoded by the patient’s visual cortex.

37 autoencoder (HNA) could in theory be used to optimize stimuli for any open-loop neuroprosthesis  
38 with a known forward model that approximates the underlying biological system.

39 In order to optimize end-to-end, the forward model must be differentiable and computationally  
40 efficient. When this is not the case, an alternative approach is to train a surrogate neural network,  
41  $\hat{f}$ , to approximate the forward model [10–13]. However, even well-trained surrogates may result in  
42 errors when included in our end-to-end framework, due to the encoders’ ability to learn to exploit the  
43 surrogate model. We therefore also evaluate whether a surrogate approach to HNA is suitable.

44 To this end, we make the following contributions:

- 45 • We propose a hybrid neural autoencoder (HNA) consisting of a deep neural encoder trained to  
46 invert a fixed, numerical or symbolic forward model (decoder) to optimize stimulus selection.  
47 Our framework is general and addresses an important challenge with sensory neuroprostheses.
- 48 • As a proof of concept, we demonstrate the utility of HNA for visual neuroprostheses, where we  
49 predict electrode activation patterns required to produce a desired visual percept. We show that  
50 the HNA is able to produce high-fidelity, patient-specific stimuli representing handwritten digits  
51 and segmented images of everyday objects, drastically outperforming conventional approaches.
- 52 • We evaluate replacing a computationally expensive or nondifferentiable forward model with a  
53 surrogate, highlighting benefits and potential dangers of popular surrogate techniques.

## 54 2 Background

55 **Sensory Neuroprostheses** Recent advances in neural understanding, wearable electronics, and  
56 biocompatible materials have accelerated the development of sensory neuroprostheses to restore  
57 perceptual function to people with impaired sensation. Use of neuroprostheses typically requires  
58 invasive implants that elicit neural responses via electrical, magnetic, or optogenetic stimulation.  
59 Two of the most promising applications are cochlear implants, which stimulate the auditory nerve to  
60 elicit sounds [3], and visual implants (see next subsection) to restore vision to the blind. However, a  
61 variety of other devices are in development; for instance, to restore touch [6, 14] or motor function  
62 [15]. The latter differ from other sensory neuroprostheses in that they generate stimuli using motor  
63 feedback (*closed loop*) [16, 17]. In the absence of feedback (*open loop*), a proper stimulus encoding  
64 is paramount to the success of these devices.

65 **Restoring Vision to the Blind** For millions of people who are living with incurable blindness, a  
66 visual prostheses (*bionic eye*, Fig. 2, left) may be the only treatment option [4]. Analogous to cochlear  
67 implants, these devices electrically stimulate surviving cells in the visual pathway to evoke visual  
68 percepts (*phosphenes*), which can support simple behavioral tasks [5, 18, 19].

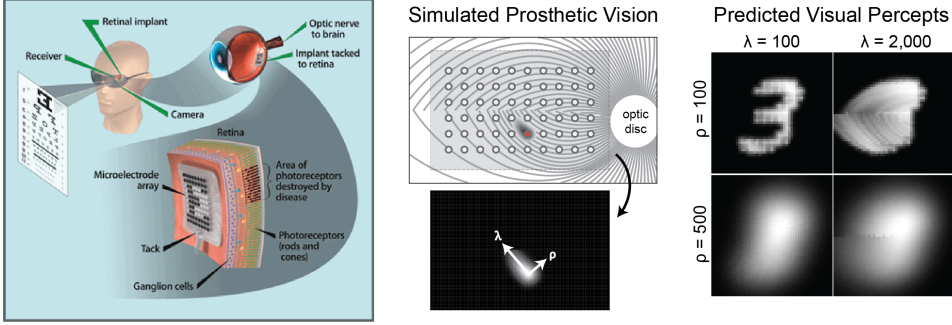


Figure 2: *Left:* Visual prosthesis. Incoming target images are transmitted from a camera to an implant in the retina, which encodes the image as an electrical stimulus pattern. *Center:* Electrical stimulation (red disc) of a nerve fiber bundle (gray lines) leads to elongated tissue activation (gray shaded region) and phosphenes whose shape can be described by two parameters,  $\lambda$  (axonal spread) and  $\rho$  (radial spread). *Right:* Predicted percepts for an MNIST digit using varying  $\rho$  and  $\lambda$  values.

69 A common misconception is that each electrode in the array can be thought of as a pixel in an image;  
70 to generate a complex visual experience, one then simply needs to turn on the right combination of  
71 pixels [20]. However, recent evidence suggests that phosphenes often appear distorted (*e.g.*, as lines,  
72 wedges, and blobs) and vary drastically across subjects and electrodes [4, 7].

73 Phosphene appearance has been best characterized in epiretinal implants, where inadvertent activation  
74 of nerve fiber bundles (NFBs) in the optic fiber layer of the retina leads to elongated phosphenes  
75 [21, 22] (Fig. 2, *center*). To this end, Granley *et al.* [23] developed a forward model to predict  
76 phosphene shape as a function of both neuroanatomical parameters (*i.e.*, location of the stimulating  
77 electrode) and stimulus parameters (*i.e.*, pulse frequency, amplitude, and duration). With this model,  
78 phosphenes are primarily characterized by two main parameters,  $\rho$  and  $\lambda$ , which dictate the size  
79 and elongation of the elicited phosphene, respectively (Fig. 2, *right*). These parameters can be  
80 determined using psychophysical tasks (*e.g.*, drawings, brightness ratings) [21, 23], and although  
81 they vary drastically across patients [21], they do not change much over time [24, 25]. Stimulation  
82 from multiple electrodes is nonlinearly integrated into a combined perception, and if two electrodes  
83 happen to activate the same NFB, they might not generate two distinct phosphenes.

### 84 3 Related Work

85 The conventional ‘naive’ encoding strategy sets the amplitude of each electrode to the brightness of  
86 the corresponding pixel in the target image [5, 26], making the stimulus a down-sampled version of  
87 the target. Although simple, this strategy only works with near-linear forward models, cannot account  
88 for real phosphene data, and often leads to unrecognizable percepts (Fig. 2, *right*) [7, 21].

89 To provide an alternative, Shah *et al.* [27] used a greedy approach to iteratively select the stimuli  
90 that best recreate a desired neural activity pattern over a given temporal window, assuming that the  
91 brain would integrate them into a coherent visual percept. Ghaffari *et al.* [28] used a neural network  
92 surrogate model combined with an interior point algorithm to optimize for localized, circular neural  
93 activation patterns for individual electrodes. Fauvel *et al.* [29] used human in-the-loop Bayesian  
94 optimization to achieve encodings perceptually favored by the subject. Spencer *et al.* [30] proposed  
95 framing the problem of stimulus encoding as inversion of a forward model of neural activation  
96 patterns, but to approximate the inverse, their approach either requires simplification or is NP-hard  
97 [30]. Furthermore, it cannot predict the perceptual consequences of the predicted neural activity.

98 Van Steveninck *et al.* [31] proposed an end-to-end optimization strategy with a fixed phosphene  
99 model, similar to HNA. However, their approach crucially differs from ours in that they included  
100 a secondary DNN to post-process the predicted phosphenes. This is a critical limitation, because a  
101 low reconstruction loss does not reveal whether a high-fidelity encoder was learned or whether the  
102 secondary decoder network simply learned to correct for the encoder’s mistakes. In addition, they  
103 used an unrealistic phosphene model that simply upscales and smooths a binary stimulus pattern. It is  
104 therefore not clear whether their results would generalize to real visual prosthesis patients.

105 Relic *et al.* [10] also utilized the end-to-end approach, but without the secondary decoder network used  
 106 in [31]. They used a more realistic phosphene model, which accounts for some spatial distortions  
 107 (*e.g.*, axonal streaks), but not the effects of stimulus parameters. Since including a nontrivial  
 108 phosphene model in the loop is not straightforward, they instead trained a surrogate neural network  
 109 to approximate the forward model. We re-implemented Relic’s surrogate approach in this paper as a  
 110 baseline method to compare against, as described in Section 4.

111 Taken together, we identified three main limitations of previous work that this study aims to address:

- 112 1) **Unrealistic forward models.** Most previous approaches (*e.g.*, [27, 30, 31]) use an overly simplified  
 113 forward model that cannot account for empirical data [7, 21]. We overcome this limitation  
 114 by developing (and inverting) a differentiable version of a neurophysiologically informed and  
 115 psychophysically validated phosphene model [23] that can account for the effects of stimulus  
 116 amplitude, frequency, and pulse duration on phosphene appearance.
- 117 2) **Optimization of neural responses.** Most previous approaches (*e.g.*, [27, 30]) focus on optimizing  
 118 neural activation patterns in the retina in response to electrical stimulation (“bottom-up”).  
 119 However, the visual system undergoes extensive remodeling during blinding diseases such as  
 120 retinitis pigmentosa [32]. Thus the link between neural activity and visual perception is unclear.  
 121 We overcome this limitation by inverting a phenomenological (“top-down”) model constrained by  
 122 behavioral data that predicts visual perception directly from electrical stimuli [21, 23].
- 123 3) **Objective function** Most previous approaches rely on minimizing mean squared error (MSE)  
 124 between the target and reconstructed image. Although simple and efficient, MSE is known to be  
 125 a poor measure of perceptual dissimilarity for images [33] and does not align well with human  
 126 assessments of image quality [34]. We overcome this limitation by proposing a joint perceptual  
 127 metric that combines mean absolute error (MAE), VGG, and Laplacian smoothing losses.

## 128 4 Methods

129 **Problem Formulation** We consider a system where there is some known forward process  $f$   
 130 mapping stimuli to responses  $f : \mathcal{S} \mapsto \mathcal{R}$ ,  $f(\mathcal{S}) \subset \mathcal{R}$ . In the case of visual prostheses,  $f$  may map  
 131 stimuli to visual percepts.  $f$  may /reviseoptionally be parameterized by patient-specific parameters  $\phi$ .

132 Finding the best stimulus for an arbitrary target response  $\mathbf{t} \in \mathcal{R}$  is equivalent to finding the inverse of  
 133  $f$ . However, since not every response can be perfectly reproduced by a stimulus, the true inverse of  $f$   
 134 is not well defined. We therefore seek the pseudoinverse (still denoted as  $f^{-1}$  for simplicity) instead,  
 135 which outputs the stimuli that produce the closest response to  $\mathbf{t}$  under some distance metric  $d$ :

$$f^{-1}(\mathbf{t}, \phi) := \arg \min_{\mathbf{s} \in \mathcal{S}} d(f(\mathbf{s}; \phi), \mathbf{t}). \quad (1)$$

136 This problem is straightforward to solve using an autoencoder approach, where a learned encoder  
 137  $f^{-1}$  is trained to invert the fixed decoder  $f$  (*i.e.*, forward model).

138 **Encoder** We approximate the pseudoinverse  $f^{-1}$  with a DNN encoder  $\hat{f}^{-1}(\mathbf{t}, \phi; \theta)$  with weights  $\theta$ ,  
 139 trained to minimize the distance  $d$  between the target image  $\mathbf{t}$  and predicted image  $\hat{\mathbf{t}}$ :

$$\min_{\theta, \phi \sim p(\phi)} d(\mathbf{t}, \hat{\mathbf{t}}) \quad (2)$$

$$\hat{\mathbf{t}} = f(\hat{f}^{-1}(\mathbf{t}, \phi; \theta); \phi), \quad (3)$$

141 where  $\phi$  is sampled from a uniform random distribution spanning the empirically observed range of  
 142 patient-specific parameters [21, 23].

143 We use a simple architecture consisting solely of fully connected (FC) and batch normalization (BN)  
 144 [35] layers (1.4M trainable parameters). First, the target  $\mathbf{t}$  is flattened and input to a FC layer. In  
 145 parallel, the patient parameters  $\phi$  are input to a BN layer and two hidden FC layers. Then, the outputs  
 146 of these two paths are concatenated, and the combined vector fed through two FC layers, producing an  
 147 intermediate representation  $\mathbf{x}$ . Amplitudes are predicted from  $\mathbf{x}$  with a FC layer. The amplitudes are  
 148 then concatenated with  $\mathbf{x}$ , put through a BN layer, and used to predict frequency and pulse duration,  
 149 each with a FC layer. The outputs are merged into a stimulus matrix  $\hat{\mathbf{s}}$ . All layers use leaky ReLU  
 150 activation, except for stimulus outputs, which use ReLU to enforce nonnegativity.

151 **Decoder** The HNA decoder is a differentiable approximation of the underlying biological system,  
 152 and describes the transform from stimulus to response. For our decoder  $f$ , we use a reformulated  
 153 but equivalent version of the model described in [23]. This model is specific to epiretinal prostheses;  
 154 analogous models exist for other neuroprostheses (*e.g.*, auditory [36–41], tactile and somatosensory  
 155 [42–46]), and could potentially be adapted for use with HNA. We use a square  $15 \times 15$  array of  
 156  $150\mu\text{m}$  electrodes, spaced  $400\mu\text{m}$  apart and centered on the fovea. The size and scale of this device  
 157 are motivated by similar designs in real epiretinal implants.

158  $f$  takes as input a stimulus matrix  $\mathbf{s} \in \mathbb{R}_{\geq 0}^{n_e \times 3}$ , where the stimulus on each electrode ( $\mathbf{s}_e$ ) is a biphasic  
 159 pulse train described by its frequency, amplitude, and pulse duration. A simulated map of retinal  
 160 NFBs is used to predict phosphene shape. Following [21], each retinal ganglion cells' activation is  
 161 assumed to be the maximum stimulation intensity along its axon. Axon sensitivity is assumed to  
 162 decay exponentially with i) distance to the stimulating electrode (radial decay rate,  $\rho$ ) and distance to  
 163 the soma along the curved axon (axonal decay rate,  $\lambda$ ). To account for stimulus properties [23],  $\rho$ ,  
 164  $\lambda$ , and the per-electrode brightness are scaled by three simple equations  $F_{\text{size}}(\mathbf{s}_e, \phi)$ ,  $F_{\text{streak}}(\mathbf{s}_e, \phi)$ ,  
 165 and  $F_{\text{bright}}(\mathbf{s}_e, \phi)$ , respectively.

166 The brightness of a pixel located at the point  $\mathbf{x} \in \mathbb{R}^2$  in the output image is given by

$$f(\mathbf{s}; \phi) = \max_{\mathbf{a} \in A} \sum_{e \in E} F_{\text{bright}}(\mathbf{s}_e, \phi) \exp \left( \frac{-\|\mathbf{x} - \mathbf{e}\|_2^2}{2\rho^2 F_{\text{size}}(\mathbf{s}_e, \phi)} + \frac{-d_s(\mathbf{x}, \mathbf{a})^2}{2\lambda^2 F_{\text{streak}}(\mathbf{s}_e, \phi)} \right) \quad (4)$$

167 where  $A$  is the cells' axon trajectory,  $E$  is the set of electrodes,  $\phi = \{\rho, \lambda, \dots\}$  is a set of 12  
 168 patient-specific parameters, and  $d_s$  is the path length along the axon trajectory [47] from  $\mathbf{a}$  to  $\mathbf{x}$ :

$$d_s(\mathbf{x}, \mathbf{a}) = \int_{\mathbf{a}}^{\mathbf{x}} \sqrt{A(\theta)^2 + \left( \frac{dA(\theta)}{d\theta} \right)^2} d\theta. \quad (5)$$

169 This model ( $f$ ) can be fit to individual patients; however, it is computationally slow and not differentiable.  
 170 For more details on these equations, see [23]. We therefore considered two approaches:

- 171 • **Differentiable Model:** We reformulated equations 4 and 5 into an equivalent set of parallelized  
 172 matrix operations, implemented in Tensorflow [48]. Significant efforts were put towards de-  
 173 veloping a model optimized for XLA engines on GPU, resulting in speedups of up to 5000x  
 174 compared to the model as presented in [23], enabling large-scale gradient descent. To enforce  
 175 differentiability, we numerically approximated  $d_s$  using  $|A| = 500$  axon segments per axon.
- 176 • **Surrogate Model:** We also implemented the surrogate approach from [10] as a baseline method,  
 177 where  $f$  is approximated with another DNN  $\hat{f}_\phi(\mathbf{s}; \theta_f)$  with weights  $\theta_f$ . To achieve this we  
 178 generated 50,000 percepts using randomly selected stimuli passed through  $f$  and fit a DNN  
 179 to produce identical images. As  $f$  is highly dependent on patient-specific parameters  $\phi$ , we  
 180 generated new data and fit a separate surrogate model for each  $\phi$  in our experimental set. Specific  
 181 implementation details of the surrogate are presented in Appendix A. Our implementation  
 182 improves upon [10] by using the more advanced phosphene model described above, which  
 183 accounts for effects of stimulus properties and allows for optimization of stimulus frequency in  
 184 addition to amplitude.

185 **Metrics** To measure perceptual similarity, we use a joint perceptual objective consisting of a VGG  
 186 [49] similarity term, a mean absolute error (MAE) term, and a smoothness regularization term. The  
 187 MAE term is given by  $L_{\text{MAE}} = \frac{1}{|\mathbf{t}|} \|\mathbf{t} - \hat{\mathbf{t}}\|_1$ .

188 The VGG term aims to capture higher-level differences between images [31, 50]. The target image  
 189 and reconstructed phosphene are input to VGG-19 pretrained on ImageNet [51], and the MSE between  
 190 the activations on a downstream convolutional layer is computed. Let  $V_l$  be a function that extracts  
 191 the activations of the  $l$ -th convolutional layer for a given image. The VGG loss is then defined as  
 192  $L_{\text{VGG}} = \frac{1}{|\mathbf{t}|} \|V_l(\mathbf{t}) - V_l(\hat{\mathbf{t}})\|_2^2$ .

193 We also include a smoothing regularization term. This term imposes a loss on the second spatial  
 194 derivative of the predicted image. A low second derivative implies that where the target image does  
 195 change, it changes slowly. We found this encouraged smoother, more connected phosphenes. To  
 196 approximate the second derivative, we convolve the image with a Laplacian filter [52] of size  $k$ ,

197 denoted by  $Lap(\cdot, k)$ , and compute the mean. The smoothness loss is given by:

$$L_{\text{Smooth}} = \frac{1}{|\hat{\mathbf{t}}|} \sum_i \left( \frac{\partial^2}{dx^2} \hat{\mathbf{t}} \right)_i = \frac{1}{|\hat{\mathbf{t}}|} \sum_i Lap(\hat{\mathbf{t}}, k)_i. \quad (6)$$

198 Our final objective is the weighted sum of the three individual losses, given by Eq. 7, where  $\alpha$  and  $\beta$   
199 are hyperparameters controlling the relative weighting of the three terms.

$$d = L_{\text{MAE}} + \alpha L_{\text{Smooth}} + \beta L_{\text{VGG}}. \quad (7)$$

200 We also implement a secondary metric to quantify phosphene recognizability, applicable only for  
201 the MNIST reconstruction task. We first pre-train a classifier network on the MNIST targets until  
202 it reaches 99% test accuracy, and then fix the weights. The relative accuracy (RA) is then defined  
203 as the ratio of the classifiers accuracy on the reconstructed images to its accuracy on the targets  
204  $RA = ACC/ACC(\mathbf{t})$ . A perfect encoder would result in  $RA = 100\%$ . A similar process was not  
205 possible for the COCO task due to the possibility of having multiple objects in each target image.

206 **Training/Optimization** We trained using Tensorflow 2.7 [48] on a single NVIDIA RTX 3090 with  
207 24GB memory. Stochastic gradient descent with Nesterov momentum was used to minimize the  
208 joint perceptual loss. We used a batch size of 16 due to memory limitations imposed by  $f$ . The  
209 amplitude, frequency predictions are scaled by 2, 20 respectively, while the pulse duration predictions  
210 were shifted by 1e-3 prior to being fed through the decoder. This encourages the initial predictions  
211 of the network to be in a reasonable range. The Laplacian filter size  $k$  is set to 5. We choose  $l$  to  
212 be first convolutional layer in the last block using cross validation (see Appendix B). Similarly, we  
213 perform cross validation to find the best values for  $\alpha$  and  $\beta$ . Instead of using one value, we found that  
214 incrementally increasing the weighting of the VGG loss ( $\beta$ ) from 0 while simultaneously decreasing  
215 the initially high weight on the smoothing constraint ( $\alpha$ ) was crucial for performance, especially  
216 when the range of allowed  $\phi$  values was large (see Appendix B).

217 **Datasets** We first evaluated on handwritten digits from MNIST [53], enabling comparison to  
218 previous works [10]. Images preprocessing consisted of resizing the target images to the same shape  
219 as the output of  $f$  (49x49). We also evaluate on more realistic images of common objects from the  
220 MS-COCO [54] dataset. We selected a subset of 25 of the MS-COCO object categories deemed  
221 more likely to be encountered by blind individuals (e.g. people, household objects), and use only  
222 images that contain at least one instance of these objects. We further filter out images by various other  
223 criteria, such as being too cluttered or too dim. This process results in a total of approximately 47K  
224 training images and 12K test images. See Appendix C for a full description of the selection process.

225 Natural images often contain too much detail to be encoded with prosthetic vision. While scene  
226 simplification strategies exist [55], we focus on the encoding algorithm, so we simply used the  
227 ground-truth segmentation masks to segment out the objects of interest. The images were then  
228 converted to grayscale, and resized to  $49 \times 49$  pixels.

## 229 5 Results

### 230 5.1 MNIST

231 The phosphenes produced from the HNA, surrogate, and naive encoders on the MNIST test set are  
232 shown in Fig. 3 and performance is summarized in Table 1. For each MNIST sample, the target  
233 image is input to the encoder, which predicts a stimulus. The stimulus is fed through the true forward  
234 model  $f$ , and the predicted phosphene is shown. Since the surrogate method must be retrained for  
235 each  $\phi$ , results are only shown for 4 simulated patients. Our proposed approach outperformed the  
236 baselines across all metrics (see Appendix D for a comparison of stimuli).

### 237 5.2 COCO

238 The phosphenes produced by HNA and the naive encoder for the segmented COCO dataset are shown  
239 in Fig. 4. We omit the surrogate results due to its poor perceptual performance on MNIST. Averaged  
240 across all  $\phi$ , HNA had a joint loss of 0.713 on the test set and MAE of 0.1408, while the naive encoder  
241 had a joint loss of 1.873 and MAE of 0.2830.

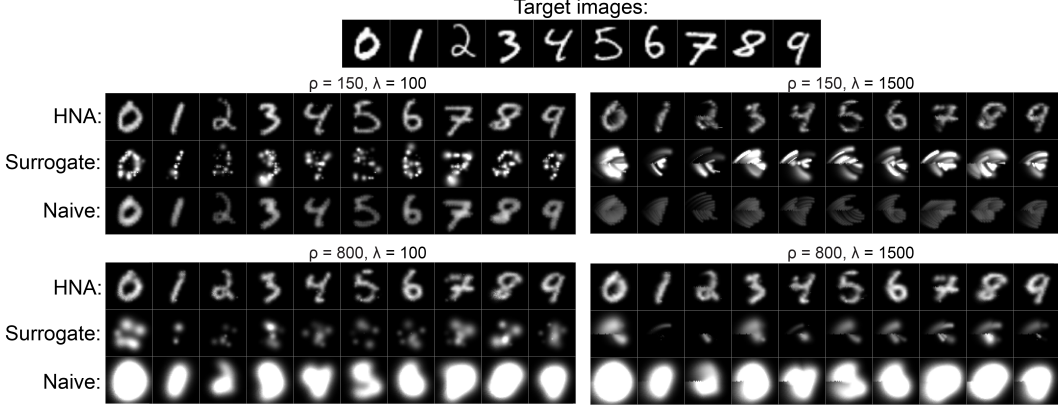


Figure 3: Reconstructed MNIST targets for HNA, surrogate, and naive encoders across 4 specific simulated patients. Note that the brightness of the naive encoder is clipped for display

Table 1: MNIST performance

Encoding	$\rho=150, \lambda=100$			$\rho=150, \lambda=1500$			$\rho=800, \lambda=100$			$\rho=800, \lambda=1500$		
	Joint Loss	MAE	RA	Joint Loss	MAE	RA	Joint Loss	MAE	RA	Joint Loss	MAE	RA
Naive	1.161	0.1855	90.3	1.442	0.214	78.1	8.152	1.500	34.8	8.780	1.726	28.8
Surrogate	2.509	0.1351	53.8	3.118	0.2431	30.7	1.692	0.2135	19.9	1.694	0.2237	18.1
HNA	<b>0.559</b>	<b>0.064</b>	<b>98.1</b>	<b>1.029</b>	<b>0.1412</b>	<b>89.3</b>	<b>0.913</b>	<b>0.113</b>	<b>95.9</b>	<b>0.957</b>	<b>0.126</b>	<b>94.8</b>

### 242 5.3 Modeling Patient-to-Patient Variations

243 MNIST encoder performance across simulated patients ( $\phi$ ) is shown in Fig. 5. Since the surrogate  
 244 encoder has to be retrained for each patient, comparison is infeasible. To visualize the effects of  
 245 changing  $\rho$  and  $\lambda$  on the produced phosphenes, Fig. 5A shows the result of encoding two example  
 246 MNIST digits, both using the naive method and our encoder. As  $\lambda$  increases, the naive phosphenes  
 247 appear increasingly elongated, and as  $\rho$  increases, the phosphenes become increasingly large and  
 248 blurry. The phosphenes from HNA are slightly too dim and disconnected at low  $\rho$ , but are relatively  
 249 stable across other values of  $\rho$  and  $\lambda$ .

250 To compare performance across the entire dataset, we computed the average test set loss across  
 251 the same range of  $\rho$  and  $\lambda$  (Fig. 5B). The encoder performs well across a wide range of simulated  
 252 patients, with larger loss only at low  $\rho$ . The naive method performs well only on a limited set of  $\phi$ ,  
 253 with small  $\lambda$  and  $\rho \approx 200$ . The naive loss was higher than the learned encoder at every simulated  
 254 point. Random sampling of  $\rho$  and  $\lambda$  for each image results in a joint loss of 0.921, MAE of 0.120,  
 255 and RA of 94.0% for HNA, while the naive encoder results in a joint loss of 3.17, MAE of 0.596, and  
 256 RA of 63.6%. The same analysis yielded similar results on COCO (Appendix E). An analysis across  
 257 other parameters is presented in Appendix F.

258 In order for prosthetic vision to be useful, different instances of the same objects would ideally  
 259 produce similar phosphenes, allowing for consistent perception. To evaluate whether our model  
 260 achieves this, we cluster the target images and resulting phosphenes using t-SNE [56] shown in  
 261 Fig. 5C. The ground truth images form clusters corresponding to the digits 0-9. The phosphenes from  
 262 our encoder roughly form similar, slightly less separated groupings, whereas the naive phosphenes do  
 263 not. To ensure that this was not the result of bad t-SNE hyperparameters, we repeated the clustering  
 264 across different perplexities and learning rates, obtaining similar or worse results.

### 265 5.4 Joint Perceptual Error Ablation Study

266 To show that the joint perceptual metric performs better than any of its individual components, we  
 267 train models using just the VGG loss and just MAE loss. Shown are values for  $\rho=150$  and  $\lambda=600$ .  
 268 As mentioned previously, encoders trained using just VGG loss fail to converge, thus we pretrain  
 269 the VGG encoder using MAE and smoothing loss, then transition to using only VGG. We do not

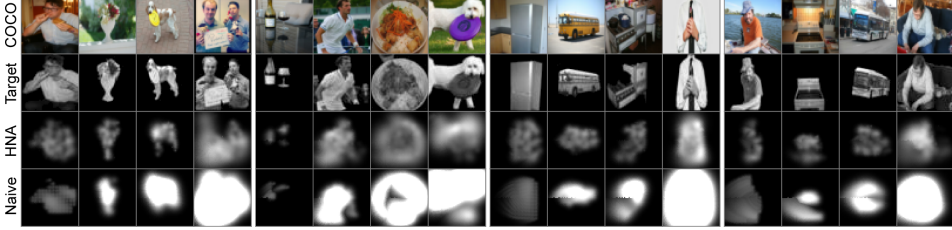


Figure 4: Original (*top row*), segmented (*second row*), and reconstructed targets for the COCO dataset, for both HNA (*third row*) and naive encoders (*bottom row*). Left to right within each block of 4 images,  $\rho$  takes values of 200, 400, 600, 800. Left to right across blocks,  $\lambda$  takes values of 250, 750, 1250, 2000. Note that the brightness of the naive method is clipped for display.

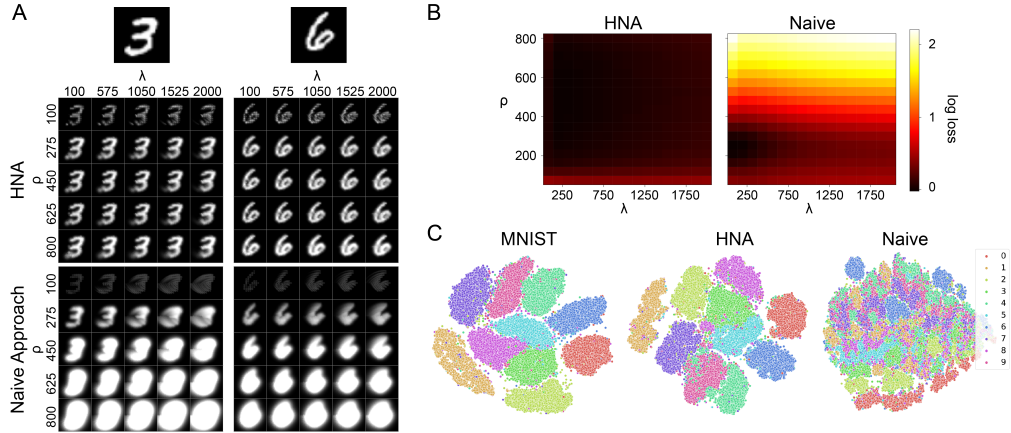


Figure 5: Encoder performance across simulated patients (varying  $\rho$  and  $\lambda$ ) on the MNIST dataset. **A:** Target, HNA encoder, and naive encoder phosphenes for two example digits. **B:** Heatmaps showing the log joint loss across  $\rho$  and  $\lambda$  for HNA and naive encoders. **C:** T-SNE clusterings on original MNIST targets, HNA reconstructed phosphenes, and naive reconstructed phosphenes.

270 consider ablating the smoothing term (Eq. 6) because it is simply a regularization term. Fig. 6 shows  
271 the phosphenes produced by HNA trained on the joint, VGG-only, and MAE-only loss.

272 The VGG encoder had a test VGG loss of 4% lower than the joint model, but its produced phosphenes  
273 are oversmoothed and blurry. The MAE encoder had a final test MAE of 9% lower than the joint  
274 model, but its produced phosphenes are disconnected and low-quality. The joint model had a RA of  
275 99.0%, the VGG encoder had a RA of 95.9%, and the joint model had a RA of 77.6%

## 276 6 Discussion

277 **Visual Prostheses** We found that HNA is able to produce high-fidelity stimuli from the MNIST  
278 and COCO datasets that outperform conventional encoding strategies across all tested conditions.  
279 Importantly, HNA produces phosphenes that are consistent across representations of the same object  
280 (Fig. 5C), which is critical to allowing prosthesis users to learn to associate certain visual patterns with  
281 specific objects. On the MNIST task, HNA produced high quality reconstructions, nearly matching  
282 the targets (Figure 3). On the harder COCO task, HNA significantly outperformed the naive encoder,  
283 but was still unable to capture all of the detail in the images. In Appendix G, we demonstrate that this  
284 is largely due to the implant’s limited spatial resolution and not a fundamental limitation of HNA.

285 Another advantage of the HNA is that it can be trained to predict stimuli across a wide range of  
286 patient-specific parameter values  $\phi$ , whereas the conventional naive encoder works well only for  
287 small values of  $\rho$  and  $\lambda$ . This may be one reason why the naive encoding strategy has been shown to  
288 lead to substantial individual differences in visual outcomes [18, 57]. Our results suggest that stimuli  
289 produced with HNA may be able to reduce at least some amount of this patient-to-patient variability.

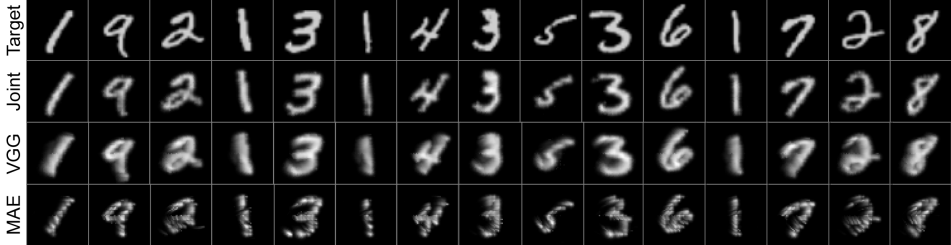


Figure 6: MNIST images for HNA encoders trained using the joint, VGG-only, and MAE-only loss.

Furthermore, HNA also proved superior to a surrogate forward model. The latter offer an alternative when the forward model is computationally expensive or not differentiable. Understandably, any inaccuracies in the surrogate model will propagate to the learned encoder during training. However, we observed that even for well trained surrogates, the encoder may still learn to exploit the inexact surrogate instead of learning to invert the true model (see Appendix A). It is possible that this exploitation could be mitigated to some extent by adversarially-robust training techniques [58]. We suspect that the surrogate method’s inferior performance here compared to [10] can be explained by our larger stimulus search space. Thus, we cannot currently suggest HNA for surrogate forward models, unless the forward model is sufficiently simple or has a small stimulus space.

**Deployment** HNA encoders must be lightweight enough to be deployed in resource-limited neuroprosthetic environments. Our encoder’s single image inference time was 1.2ms on GPU and 4ms on CPU. Future work could reduce these numbers through network pruning, mixed precision, and architecture search. Low-power Edge AI accelerators (*e.g.*, Intel’s Neural Compute Stick) and dedicated neuromorphic hardware (*e.g.*, BrainChip’s Akida SoC) may provide another solution.

**Broader Impacts** While our work is presented in the context of visual prostheses, the HNA framework may apply to any sensory neuroprosthesis where stimulus selection can be informed by a numeric or symbolic forward model. For example, HNA could be used in cochlear implants [3] to choose stimuli that result in a desired sound, and in spinal cord implants [15] to find the best way to relay neural signals through a damaged section of the spinal cord. Conveniently, the forward models required by HNA have already been developed for a range of applications [36–46]. However, HNA might not apply to all neural interfaces, such as systems without a clear neural or perceptual target (*e.g.*, deep brain stimulation for the treatment of Parkinson’s [59]) or closed-loop systems [16, 60].

**Limitations** Despite HNA’s potential, the current implementation has a number of limitations. First, as presented the HNA encoder only applies to static targets. Hence dynamic targets must be split into individual frames and encoded separately. However, one approach might be to encode entire stimulus sequences (instead of frames) that are optimized to reconstruct the dynamic target sequence.

Second, HNA works best if there is an accurate forward model mapping from stimulus space to perception. However, Appendix H shows that HNA may still give benefits over a naive encoding even when patient-specific parameters are unknown or mis-specified. In general, if a prosthesis elicits similar results across patients, then a non-patient-specific model would suffice.

Third, the current work deals only with simulated patients. The use of a DNN for stimulus encoding in real patients may raise safety concerns. Since we cannot examine the process by which stimuli are chosen, it is possible that HNA might produce harmful stimuli that could lead to serious adverse events (*e.g.*, seizures). However, this concern is mitigated by the fact that most neuroprostheses are equipped with firmware responsible for ensuring stimuli stay within FDA-approved safety limits.

## 7 Conclusion

In summary, this paper proposes a hybrid autoencoder structure as a general framework for stimulus optimization in sensory neuroprostheses and, as a proof of concept, demonstrates its utility on the prominent example of visual neuroprostheses, drastically outperforming conventional encoding strategies. This may prove a promising solution for a variety of neuroprosthetic technologies.

330 **References**

- 331 [1] Caterina Cinel, Davide Valeriani, and Riccardo Poli. Neurotechnologies for Human Cognitive Augmen-  
332 tation: Current State of the Art and Future Prospects. *Frontiers in Human Neuroscience*, 13:13, January  
333 2019.
- 334 [2] Eduardo Fernandez. Development of visual Neuroprostheses: trends and challenges. *Bioelectronic  
335 Medicine*, 4(1):12, August 2018.
- 336 [3] Blake S. Wilson, Charles C. Finley, Dewey T. Lawson, Robert D. Wolford, Donald K. Eddington, and  
337 William M. Rabinowitz. Better speech recognition with cochlear implants. *Nature*, 352(6332):236–238,  
338 July 1991. Number: 6332 Publisher: Nature Publishing Group.
- 339 [4] Eduardo Fernández, Arantxa Alfaro, Cristina Soto-Sánchez, Pablo Gonzalez-Lopez, Antonio M. Lozano,  
340 Sebastian Peña, María Dolores Grima, Alfonso Rodil, Bernardeta Gómez, Xing Chen, Pieter R. Roelfsema,  
341 John D. Rolston, Tyler S. Davis, and Richard A. Normann. Visual percepts evoked with an intracortical  
342 96-channel microelectrode array inserted in human occipital cortex. *Journal of Clinical Investigation*,  
343 131(23):e151331, December 2021.
- 344 [5] Yvonne Hsu-Lin Luo and Lyndon da Cruz. The Argus® II Retinal Prosthesis System. *Progress in Retinal  
345 and Eye Research*, 50:89–107, January 2016.
- 346 [6] Daniel W. Tan, Matthew A. Schiefer, Michael W. Keith, James Robert Anderson, Joyce Tyler, and  
347 Dustin J. Tyler. A neural interface provides long-term stable natural touch perception. *Science Transla-  
348 tional Medicine*, 6(257):257ra138–257ra138, October 2014. Publisher: American Association for the  
349 Advancement of Science.
- 350 [7] Cordelia Erickson-Davis and Helma Korzybska. What do blind people “see” with retinal prostheses?  
351 Observations and qualitative reports of epiretinal implant users. *PLOS ONE*, 16(2):e0229189, February  
352 2021. Publisher: Public Library of Science.
- 353 [8] Craig D. Murray. Embodiment and Prosthetics. In Pamela Gallagher, Deirdre Desmond, and Malcolm  
354 MacLachlan, editors, *Psychoprosthetics*, pages 119–129. Springer, London, 2008.
- 355 [9] Bingni W. Brunton and Michael Beyeler. Data-driven models in human neuroscience and neuroengineering.  
356 *Current Opinion in Neurobiology*, 58:21–29, October 2019.
- 357 [10] Lucas Relic, Bowen Zhang, Yi-Lin Tuan, and Michael Beyeler. Deep Learning-Based Perceptual Stimulus  
358 Encoder for Bionic Vision. In *Augmented Humans 2022*, AHs 2022, pages 323–325, New York, NY, USA,  
359 March 2022. Association for Computing Machinery.
- 360 [11] David Montes de Oca Zapiain, James A. Stewart, and Rémi Dingreville. Accelerating phase-field-based  
361 microstructure evolution predictions via surrogate models trained by machine learning methods. *npj  
362 Computational Materials*, 7(1):1–11, January 2021. Number: 1 Publisher: Nature Publishing Group.
- 363 [12] Mohammad Amin Nabian and Hadi Meidani. A Deep Neural Network Surrogate for High-Dimensional  
364 Random Partial Differential Equations. *Probabilistic Engineering Mechanics*, 57:14–25, July 2019.  
365 arXiv:1806.02957 [physics, stat].
- 366 [13] Stefanos Nikolopoulos, Ioannis Kalogeris, and Vissarion Papadopoulos. Non-intrusive surrogate mod-  
367 eling for parametrized time-dependent partial differential equations using convolutional autoencoders.  
368 *Engineering Applications of Artificial Intelligence*, 109:104652, March 2022.
- 369 [14] Gregg A. Tabot, John F. Dammann, Joshua A. Berg, Francesco V. Tenore, Jessica L. Boback, R. Jacob  
370 Vogelstein, and Sliman J. Bensmaia. Restoring the sense of touch with a prosthetic hand through a brain  
371 interface. *Proceedings of the National Academy of Sciences*, 110(45):18279–18284, November 2013.
- 372 [15] Marco Capogrosso, Tomislav Milekovic, David Borton, Fabien Wagner, Eduardo Martin Moraud, Jean-  
373 Baptiste Mignardot, Nicolas Buse, Jerome Gandar, Quentin Barraud, David Xing, Elodie Rey, Simone  
374 Duis, Yang Jianzhong, Wai Kin D. Ko, Qin Li, Peter Detemple, Tim Denison, Silvestro Micera, Erwan  
375 Bezard, Jocelyne Bloch, and Grégoire Courtine. A brain-spine interface alleviating gait deficits after spinal  
376 cord injury in primates. *Nature*, 539(7628):284–288, November 2016.
- 377 [16] Christopher A. R. Chapman, Noah Goshi, and Erkin Seker. Multifunctional Neural Interfaces for Closed-  
378 Loop Control of Neural Activity. *Advanced Functional Materials*, 28(12):1703523, 2018. \_eprint:  
379 <https://onlinelibrary.wiley.com/doi/pdf/10.1002/adfm.201703523>.

- 380 [17] Fabien B. Wagner, Jean-Baptiste Mignardot, Camille G. Le Goff-Mignardot, Robin Demesmaeker, Salif  
 381 Komi, Marco Capogrosso, Andreas Rowald, Ismael Seáñez, Miroslav Caban, Elvira Pirondini, Molywan  
 382 Vat, Laura A. McCracken, Roman Heimgartner, Isabelle Fodor, Anne Watrin, Perrine Seguin, Edoardo  
 383 Paoles, Katrien Van Den Keybus, Grégoire Eberle, Brigitte Schurch, Etienne Pralong, Fabio Becce, John  
 384 Prior, Nicholas Buse, Rik Buschman, Esra Neufeld, Niels Kuster, Stefano Carda, Joachim von Zitzewitz,  
 385 Vincent Delattre, Tim Denison, Hendrik Lambert, Karen Minassian, Jocelyne Bloch, and Grégoire Courtine.  
 386 Targeted neurotechnology restores walking in humans with spinal cord injury. *Nature*, 563(7729):65–71,  
 387 November 2018.
- 388 [18] Katarina Stingl, Ruth Schippert, Karl U. Bartz-Schmidt, Dorothea Besch, Charles L. Cottrall, Thomas L.  
 389 Edwards, Florian Gekeler, Udo Greppmaier, Katja Kiel, Assen Koitschev, Laura Kühlewein, Robert E.  
 390 MacLaren, James D. Ramsden, Johann Roider, Albrecht Rothermel, Helmut Sachs, Greta S. Schröder,  
 391 Jan Tode, Nicole Troelenberg, and Eberhart Zrenner. Interim Results of a Multicenter Trial with the New  
 392 Electronic Subretinal Implant Alpha AMS in 15 Patients Blind from Inherited Retinal Degenerations.  
 393 *Frontiers in Neuroscience*, 11, 2017. Publisher: Frontiers.
- 394 [19] Lewis Karapanos, Carla J. Abbott, Lauren N. Ayton, Maria Kolic, Myra B. McGuinness, Elizabeth K.  
 395 Baglin, Samuel A. Titchener, Jessica Kvansakul, Dean Johnson, William G. Kentler, Nick Barnes, David  
 396 A. X. Nayagam, Penelope J. Allen, and Matthew A. Petoe. Functional Vision in the Real-World Environ-  
 397 ment With a Second-Generation (44-Channel) Suprachoroidal Retinal Prosthesis. *Translational Vision  
 398 Science & Technology*, 10(10):7–7, August 2021. Publisher: The Association for Research in Vision and  
 399 Ophthalmology.
- 400 [20] Wm H. Dobelle. Artificial Vision for the Blind by Connecting a Television Camera to the Visual Cortex.  
 401 *ASAIO Journal*, 46(1):3–9, February 2000.
- 402 [21] Michael Beyeler, Devyani Nanduri, James D. Weiland, Ariel Rokem, Geoffrey M. Boynton, and Ione Fine.  
 403 A model of ganglion axon pathways accounts for percepts elicited by retinal implants. *Scientific Reports*,  
 404 9(1):1–16, June 2019.
- 405 [22] J. F. Rizzo, J. Wyatt, J. Loewenstein, S. Kelly, and D. Shire. Perceptual efficacy of electrical stimulation  
 406 of human retina with a microelectrode array during short-term surgical trials. *Invest Ophthalmol Vis Sci*,  
 407 44(12):5362–9, December 2003.
- 408 [23] Jacob Granley and Michael Beyeler. A Computational Model of Phosphene Appearance for Epiretinal  
 409 Prostheses. In *2021 43rd Annual International Conference of the IEEE Engineering in Medicine Biology  
 410 Society (EMBC)*, pages 4477–4481, November 2021. ISSN: 2694-0604.
- 411 [24] Yvonne H-L. Luo, Joe Jiangjian Zhong, Monica Clemo, and Lyndon da Cruz. Long-term Repeatability  
 412 and Reproducibility of Phosphene Characteristics in Chronically Implanted Argus II Retinal Prosthesis  
 413 Subjects. *American Journal of Ophthalmology*, 170:100–109, October 2016.
- 414 [25] M. Beyeler, A. Rokem, G. M. Boynton, and I. Fine. Learning to see again: biological constraints on  
 415 cortical plasticity and the implications for sight restoration technologies. *J Neural Eng*, 14(5):051003, June  
 416 2017.
- 417 [26] S. C. Chen, G. J. Suaning, J. W. Morley, and N. H. Lovell. Simulating prosthetic vision: I. Visual models  
 418 of phosphenes. *Vision Research*, 49(12):1493–506, June 2009.
- 419 [27] Nishal P. Shah, Sasidhar Madugula, Lauren Grosberg, Gonzalo Mena, Pukit Tandon, Pawel Hottowy,  
 420 Alexander Sher, Alan Litke, Subhasish Mitra, and E.J. Chichilnisky. Optimization of Electrical Stimulation  
 421 for a High-Fidelity Artificial Retina. In *2019 9th International IEEE/EMBS Conference on Neural  
 422 Engineering (NER)*, pages 714–718, March 2019. ISSN: 1948-3554.
- 423 [28] Dorsa Haji Ghaffari, Yao-Chuan Chang, Ehsan Mirzakhaili, and James D. Weiland. Closed-loop Opti-  
 424 mization of Retinal Ganglion Cell Responses to Epiretinal Stimulation: A Computational Study. In *2021  
 425 10th International IEEE/EMBS Conference on Neural Engineering (NER)*, pages 597–600, May 2021.  
 426 ISSN: 1948-3554.
- 427 [29] Tristan Fauvel and Matthew Chalk. Human-in-the-loop optimization of visual prosthetic stimulation.  
 428 preprint, Neuroscience, November 2021.
- 429 [30] Martin J. Spencer, Tatiana Kameneva, David B. Grayden, Hamish Meffin, and Anthony N. Burkitt. Global  
 430 activity shaping strategies for a retinal implant. *Journal of Neural Engineering*, 16(2):026008, January  
 431 2019. Publisher: IOP Publishing.
- 432 [31] Jaap de Ruyter van Steveninck, Umut Güçlü, Richard van Wezel, and Marcel van Gerven. End-to-end  
 433 optimization of prosthetic vision. *Journal of Vision*, 22(2):20, February 2022.

- 434 [32] Robert E Marc, Bryan W Jones, Carl B Watt, and Enrica Strettoi. Neural remodeling in retinal degeneration.  
 435 *Progress in Retinal and Eye Research*, 22(5):607–655, 2003.
- 436 [33] Zhou Wang and Alan C. Bovik. Mean squared error: Love it or leave it? A new look at Signal Fidelity  
 437 Measures. *IEEE Signal Processing Magazine*, 26(1):98–117, January 2009. Conference Name: IEEE  
 438 Signal Processing Magazine.
- 439 [34] Guangtao Zhai and Xiongkuo Min. Perceptual image quality assessment: a survey. *Science China  
 440 Information Sciences*, 63(11):211301, November 2020.
- 441 [35] Sergey Ioffe and Christian Szegedy. Batch Normalization: Accelerating Deep Network Training by Reduc-  
 442 ing Internal Covariate Shift. Technical Report arXiv:1502.03167, arXiv, March 2015. arXiv:1502.03167  
 443 [cs] type: article.
- 444 [36] Michael F Dorman, Anthony J Spahr, Philipos C Loizou, Cindy J Dana, and Jennifer S Schmidt. Acoustic  
 445 simulations of combined electric and acoustic hearing (eas). *Ear and Hearing*, 26(4):371–380, 2005.
- 446 [37] Mario A Svirsky, Nai Ding, Elad Sagi, Chin-Tuan Tan, Matthew Fitzgerald, E Katelyn Glassman, Keena  
 447 Seward, and Arlene C Neuman. Validation of acoustic models of auditory neural prostheses. In *2013 IEEE  
 448 International Conference on Acoustics, Speech and Signal Processing*, pages 8629–8633. IEEE, 2013.
- 449 [38] MF Dorman, PC Loizou, A Spahr, and CJ Dana. Simulations of combined acoustic/electric hearing. In  
 450 *Proceedings of the 25th Annual International Conference of the IEEE Engineering in Medicine and Biology  
 451 Society (IEEE Cat. No. 03CH37439)*, volume 3, pages 1999–2001. IEEE, 2003.
- 452 [39] Michael F Dorman, Philipos C Loizou, and Dawne Rainey. Speech intelligibility as a function of the  
 453 number of channels of stimulation for signal processors using sine-wave and noise-band outputs. *The  
 454 Journal of the Acoustical Society of America*, 102(4):2403–2411, 1997.
- 455 [40] William B Cooper, Emily Tobey, and Philipos C Loizou. Music perception by cochlear implant and normal  
 456 hearing listeners as measured by the montreal battery for evaluation of amusia. *Ear and hearing*, 29(4):618,  
 457 2008.
- 458 [41] Philipos C Loizou, Michael Dorman, Oguz Poroy, and Tony Spahr. Speech recognition by normal-hearing  
 459 and cochlear implant listeners as a function of intensity resolution. *The Journal of the Acoustical Society  
 460 of America*, 108(5):2377–2387, 2000.
- 461 [42] Hannes P Saal, Benoit P Delhaye, Brandon C Rayhaun, and Sliman J Bensmaia. Simulating tactile signals  
 462 from the whole hand with millisecond precision. *Proceedings of the National Academy of Sciences*,  
 463 114(28):E5693–E5702, 2017.
- 464 [43] Elizaveta V Okorokova, Qinpu He, and Sliman J Bensmaia. Biomimetic encoding model for restoring  
 465 touch in bionic hands through a nerve interface. *Journal of neural engineering*, 15(6):066033, 2018.
- 466 [44] Douglas J Weber, Rebecca Friesen, and Lee E Miller. Interfacing the somatosensory system to restore  
 467 touch and proprioception: essential considerations. *Journal of motor behavior*, 44(6):403–418, 2012.
- 468 [45] Sung Soo Kim, Arun P Sripathi, and Sliman J Bensmaia. Predicting the timing of spikes evoked by tactile  
 469 stimulation of the hand. *Journal of neurophysiology*, 104(3):1484–1496, 2010.
- 470 [46] Milana P Mileusnic, Ian E Brown, Ning Lan, and Gerald E Loeb. Mathematical models of proprioceptors.  
 471 i. control and transduction in the muscle spindle. *Journal of neurophysiology*, 96(4):1772–1788, 2006.
- 472 [47] N. M. Janssonius, J. Nevalainen, B. Selig, L. M. Zangwill, P. A. Sample, W. M. Budde, J. B. Jonas,  
 473 W. A. Lagrèze, P. J. Airaksinen, R. Vonthein, L. A. Levin, J. Paetzold, and U. Schiefer. A mathematical  
 474 description of nerve fiber bundle trajectories and their variability in the human retina. *Vision Research*,  
 475 49(17):2157–2163, August 2009.
- 476 [48] Martín Abadi, Ashish Agarwal, Paul Barham, Eugene Brevdo, Zhifeng Chen, Craig Citro, Greg S. Corrado,  
 477 Andy Davis, Jeffrey Dean, Matthieu Devin, Sanjay Ghemawat, Ian Goodfellow, Andrew Harp, Geoffrey  
 478 Irving, Michael Isard, Yangqing Jia, Rafal Jozefowicz, Lukasz Kaiser, Manjunath Kudlur, Josh Levenberg,  
 479 Dandelion Mané, Rajat Monga, Sherry Moore, Derek Murray, Chris Olah, Mike Schuster, Jonathon Shlens,  
 480 Benoit Steiner, Ilya Sutskever, Kunal Talwar, Paul Tucker, Vincent Vanhoucke, Vijay Vasudevan, Fernanda  
 481 Viégas, Oriol Vinyals, Pete Warden, Martin Wattenberg, Martin Wicke, Yuan Yu, and Xiaoqiang Zheng.  
 482 TensorFlow: Large-scale machine learning on heterogeneous systems, 2015. Software available from  
 483 tensorflow.org.
- 484 [49] Karen Simonyan and Andrew Zisserman. Very Deep Convolutional Networks for Large-Scale Image  
 485 Recognition. Technical Report arXiv:1409.1556, arXiv, April 2015. arXiv:1409.1556 [cs] type: article.

- 486 [50] Yijun Li, Chen Fang, Jimei Yang, Zhaowen Wang, Xin Lu, and Ming-Hsuan Yang. Universal Style  
 487 Transfer via Feature Transforms. In *Advances in Neural Information Processing Systems*, volume 30.  
 488 Curran Associates, Inc., 2017.
- 489 [51] Jia Deng, Wei Dong, Richard Socher, Li-Jia Li, Kai Li, and Li Fei-Fei. ImageNet: A large-scale hierarchical  
 490 image database. In *2009 IEEE Conference on Computer Vision and Pattern Recognition*, pages 248–255,  
 491 June 2009. ISSN: 1063-6919.
- 492 [52] Sylvain Paris, Samuel W Hasinoff, and Jan Kautz. Local Laplacian Filters: Edge-aware Image Processing  
 493 with a Laplacian Pyramid. *Communications of the ACM*, 58:11, 2015.
- 494 [53] Li Deng. The mnist database of handwritten digit images for machine learning research. *IEEE Signal  
 495 Processing Magazine*, 29(6):141–142, 2012.
- 496 [54] Tsung-Yi Lin, Michael Maire, Serge Belongie, Lubomir Bourdev, Ross Girshick, James Hays, Pietro  
 497 Perona, Deva Ramanan, C. Lawrence Zitnick, and Piotr Dollár. Microsoft COCO: Common Objects in  
 498 Context. Technical Report arXiv:1405.0312, arXiv, February 2015. arXiv:1405.0312 [cs] type: article.
- 499 [55] Nicole Han, Sudhanshu Srivastava, Aiwen Xu, Devi Klein, and Michael Beyeler. Deep Learning-Based  
 500 Scene Simplification for Bionic Vision. In *Augmented Humans Conference 2021*, AHs’21, pages 45–54,  
 501 New York, NY, USA, February 2021. Association for Computing Machinery.
- 502 [56] Laurens Van der Maaten and Geoffrey Hinton. Visualizing data using t-sne. *Journal of machine learning  
 503 research*, 9(11), 2008.
- 504 [57] Eli Peli. Testing Vision Is Not Testing For Vision. *Translational Vision Science & Technology*, 9(13):32–32,  
 505 December 2020. Publisher: The Association for Research in Vision and Ophthalmology.
- 506 [58] Florian Tramèr, Alexey Kurakin, Nicolas Papernot, Ian Goodfellow, Dan Boneh, and Patrick McDaniel.  
 507 Ensemble adversarial training: Attacks and defenses. *arXiv preprint arXiv:1705.07204*, 2017.
- 508 [59] Alim Louis Benabid. Deep brain stimulation for Parkinson’s disease. *Current Opinion in Neurobiology*,  
 509 13(6):696–706, December 2003.
- 510 [60] Bardia Bozorgzadeh, Douglas R. Schuweiler, Martin J. Bobak, Paul A. Garris, and Pedram Mohseni.  
 511 Neurochemostat: A Neural Interface SoC With Integrated Chemometrics for Closed-Loop Regulation of  
 512 Brain Dopamine. *IEEE Transactions on Biomedical Circuits and Systems*, 10(3):654–667, June 2016.  
 513 Conference Name: IEEE Transactions on Biomedical Circuits and Systems.
- 514 [61] M. Beyeler, G. M. Boynton, I. Fine, and A. Rokem. pulse2percept: A Python-based simulation framework  
 515 for bionic vision. In K. Huff, D. Lippa, D. Niederhut, and M. Pacer, editors, *Proceedings of the 16th  
 516 Science in Python Conference*, pages 81–88, 2017.
- 517 [62] Ilya Loshchilov and Frank Hutter. Decoupled weight decay regularization. *arXiv preprint  
 518 arXiv:1711.05101*, 2017.

519    **Checklist**

- 520    1. For all authors...
  - 521    (a) Do the main claims made in the abstract and introduction accurately reflect the paper's  
522    contributions and scope? **[Yes]**
  - 523    (b) Did you describe the limitations of your work? **[Yes]** we highlight both the limitations  
524    of our general framework and our specific proof of concept, see Section 6
  - 525    (c) Did you discuss any potential negative societal impacts of your work? **[Yes]** See  
526    Section 6, last paragraph
  - 527    (d) Have you read the ethics review guidelines and ensured that your paper conforms to  
528    them? **[Yes]**
- 529    2. If you are including theoretical results...
  - 530    (a) Did you state the full set of assumptions of all theoretical results? **[N/A]** We do not  
531    present any theoretical results
  - 532    (b) Did you include complete proofs of all theoretical results? **[N/A]**
- 533    3. If you ran experiments...
  - 534    (a) Did you include the code, data, and instructions needed to reproduce the main experi-  
535    mental results (either in the supplemental material or as a URL)? **[Yes]** We include  
536    the trained models, and code to reproduce the main result figures in the supplementary  
537    materials.
  - 538    (b) Did you specify all the training details (e.g., data splits, hyperparameters, how they  
539    were chosen)? **[Yes]** detailed instructions are given in 4, training paragraph on  
540    hyperparameter selection, learning rates, and many other training details. Data splits  
541    were predetermined by the datasets (MNIST and COCO already have splits), with some  
542    more details given in Appendix C
  - 543    (c) Did you report error bars (e.g., with respect to the random seed after running experi-  
544    ments multiple times)? **[No]** We do not train our models multiple times. Once trained,  
545    the networks produce consistent results.
  - 546    (d) Did you include the total amount of compute and the type of resources used (e.g., type  
547    of GPUs, internal cluster, or cloud provider)? **[Yes]** This is specified in Section 4,  
548    training paragraph
- 549    4. If you are using existing assets (e.g., code, data, models) or curating/releasing new assets...
  - 550    (a) If your work uses existing assets, did you cite the creators? **[Yes]** We used models  
551    from [10, 21, 23], which are all cited whenever used in the paper.
  - 552    (b) Did you mention the license of the assets? **[N/A]**
  - 553    (c) Did you include any new assets either in the supplemental material or as a URL? **[Yes]**  
554    , we provide saved weights for our final trained models, along with code to display  
555    results shown on main results figures.
  - 556    (d) Did you discuss whether and how consent was obtained from people whose data you're  
557    using/curating? **[N/A]** We do not use any new personal data
  - 558    (e) Did you discuss whether the data you are using/curating contains personally identifiable  
559    information or offensive content? **[N/A]** The data used does not contain any identifying  
560    information or offensive content.
- 561    5. If you used crowdsourcing or conducted research with human subjects...
  - 562    (a) Did you include the full text of instructions given to participants and screenshots, if  
563    applicable? **[N/A]**
  - 564    (b) Did you describe any potential participant risks, with links to Institutional Review  
565    Board (IRB) approvals, if applicable? **[N/A]**
  - 566    (c) Did you include the estimated hourly wage paid to participants and the total amount  
567    spent on participant compensation? **[N/A]**

568 **Appendix**

569 **A Surrogate Model**

570 This section covers specific implementation details about the surrogate model as well as observations  
 571 on its performance.

572 **A.1 Implementation Details**

573 **Dataset** To create training data for the surrogate model  $\hat{f}_\phi$ , we used the phosphene model described  
 574 in [23] and implemented in pulse2percept v0.8 [61]. 50,000 stimuli were created by first selecting  
 575 a number of electrodes to stimulate between 1 and 30 randomly chosen electrodes, then randomly  
 576 selecting an amplitude between 1 and 10 (specified as a multiple of the assumed threshold current)  
 577 and frequency between 1 and 200 Hz for each electrode. In addition, between 10 and 100 electrodes  
 578 were chosen to act as “noise” electrodes, where either amplitude or frequency was given a nonzero  
 579 value, but not both. The purpose of these electrodes was for the surrogate model to learn that  
 580 both a nonzero amplitude and a nonzero frequency are required to produce a visible percept. We  
 581 used an 80-20 train-test split. As the surrogate model is highly dependent on patient-specific  
 582 parameters  $\phi$ , we generated new data and fit a separate surrogate for each of the following  $\phi$ :  
 583  $((\rho, \lambda) \in \{(150, 100), (150, 1500), (800, 100), (800, 1500)\})$ .

584 **Network Architecture** The surrogate model  $\hat{f}_\phi$  used a fully-connected architecture. The input to  
 585 the model was a stimulus matrix  $s \in \mathbb{R}_{\geq 0}^{n_{ex} \times 3}$ , which was identical to the input to  $f$ . The stimulus  
 586 matrix was split into amplitude and frequency components (pulse duration was not used due to  
 587 poor model performance), which were fed through a FC layer. The outputs of both FC layers were  
 588 concatenated and fed through another FC layer. Concurrently, the model computed the element-wise  
 589 product of the amplitude and frequency components and passed it through a separate FC layer. The  
 590 outputs of the previous two layers were then concatenated and fed through a final FC layer with  
 591 output size  $49 \times 49$ .

592 The model was trained for 45 epochs using AdamW [62] optimizer and MAE loss.

593 **A.2 Approximating the Forward Model**

594 The surrogate model was able to accurately approximate the true phosphene model  $f$ . Table 2 shows  
 595 MAE over the validation set (10,000 percepts) for all 4 trained  $\hat{f}_\phi$ . Visually, the predicted percepts  
 596 were nearly identical to the ground truth.

Table 2: Surrogate model performance

$\phi$	$\rho = 150 \lambda = 100$	$\rho = 150 \lambda = 1500$	$\rho = 800 \lambda = 100$	$\rho = 800 \lambda = 1500$
MAE	0.0119	0.0189	0.0078	0.0115

597 **A.3 Predicted Stimuli**

598 Despite the low surrogate validation error, training with the surrogate model would often result in the  
 599 encoder suggesting almost adversarial stimuli; that is, stimuli that if fed through the true forward  
 600 model  $f$  would lead to drastically different percepts than if fed through the surrogate model  $\hat{f}$  (see  
 601 Fig. A.1). With these adversarial-like stimuli, the encoder appears to be performing well under the  
 602 surrogate model, but performs poorly when the same stimuli are input to the true forward model. We  
 603 identify this as the primary disadvantage of using a surrogate model and resolving this issue remains  
 604 an open research problem for end-to-end training with surrogate methods.

605 We noticed several issues caused by the effects of varying stimulus parameters on phosphene  
 606 appearance. For example, increasing amplitude increases size and brightness, while increasing  
 607 frequency increases brightness only. We noticed a larger mismatch between the surrogate and the  
 608 forward model on the extreme ends of the spectrum (*e.g.* very high frequency, low amplitude),

609 resulting in the encoder settling into a minimum that does not exist in the true forward model. It  
 610 is important to note this disparity appears despite a high training accuracy of the surrogate alone.  
 611 Although these examples are specific to the bionic vision application, we expect surrogate models  
 612 derived to describe other neuromodulation technologies to suffer from similar limitations.

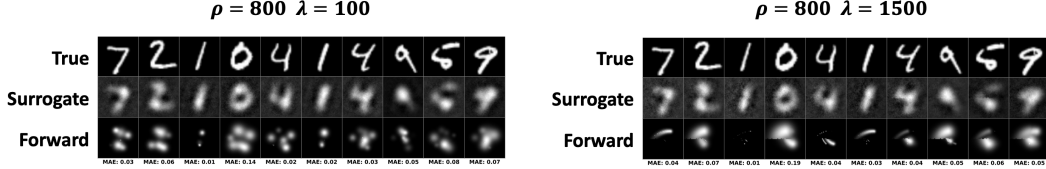


Figure A.1: The encoder would often suggest stimuli that lead to drastically different percepts when fed through the surrogate model ( $\hat{f}$ , middle row) as compared to the true forward model ( $f$ , bottom row). Examples are shown for  $\rho = 800$ ;  $\lambda = 100$  (left) and  $\rho = 800$   $\lambda = 1500$  (right).

613 **B Hyperparameter Selection**

614 In this section, we detail how HNA hyperparameters ( $l$ ,  $k$ ,  $\alpha$ , and  $\beta$ ) were chosen.

615 **VGG Loss** To choose the layer of the VGG network to use for VGG loss ( $l$ ) we performed cross  
 616 validation across a set of candidate layers. Previous studies [50] have shown that the first layer with  
 617 each of the 5 convolutional blocks perform well for neural style transfer. Thus, we choose these as  
 618 our candidate layers. For cross validation, we trained HNA for 50 epochs using each candidate layer.  
 619 The resulting phosphenes are shown in Figure B.1. Using earlier layers, the VGG term performs  
 620 similarly to MAE, and phosphenes are disconnected. We chose layer 5\_1 based on its perceived  
 621 ability to capture high-level perceptual differences between images, although layer 4\_1 also performs  
 622 similarly.

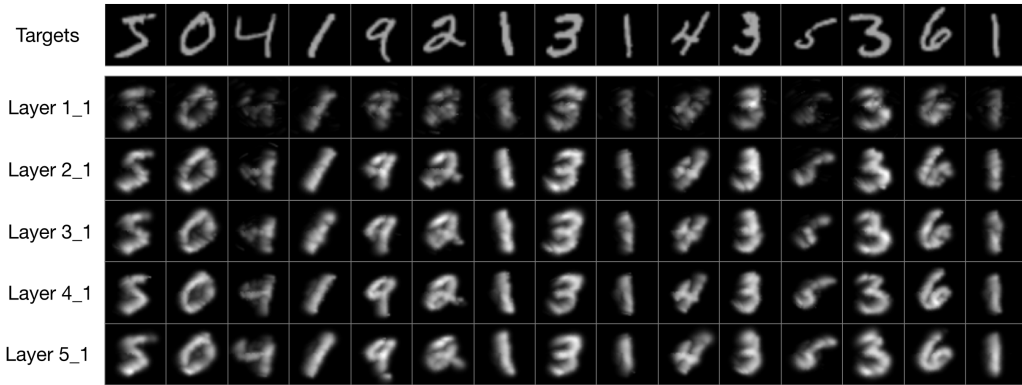


Figure B.1: Phosphenes produced by HNA encoder with different layers chosen for VGG loss. Layer 5\_1 denotes the first layer within the fifth convolutional block.

623 **Laplacian Smoothing** We chose to use a kernel size 5 for the Laplacian filter used to estimate the  
 624 second derivative ( $k$ , Eq. 6). The size of the filter controls the scale on which smoothing is applied  
 625 (*i.e.*, smaller filters sizes only encourage continuity within a small local region, whereas larger filters  
 626 encourage continuity within a larger region). Size 5 was chosen because larger filters were observed  
 627 to over-smooth the image, while smaller filters still led to highly disconnected phosphenes.

628 **Joint Perceptual Metric** We performed cross validation to find the best values for  $\alpha$  and  $\beta$ . Instead  
 629 of using one value, we found scheduled weighting to be crucial for performance. The scheduler  
 630 incrementally increased the weight of the VGG loss ( $\beta$ ) from 0 while simultaneously decreasing the  
 631 initially high weight on the smoothing constraint ( $\alpha$ ). This was motivated by the observation that the  
 632 VGG loss performed poorly during early iterations when the predicted phophene was near-random.

633 Under this scheduled weighting strategy, the loss is dominated early on by the MAE and smoothing  
 634 terms. This encourages the model to just output reasonable encodings. As training progresses, the  
 635 predicted phosphenes become higher quality, causing the VGG loss to perform better, and thus the  
 636 smoothing term is no longer as important.

637 Additionally, we found it beneficial to temporarily decrease the learning rate by a factor of 10 for a  
 638 short 'warm-up' duration following each increase in  $\beta$ , before resetting to 50% of the prior learning  
 639 rate. This results in the learning rate gradually decreasing throughout training by a factor of around  
 640 100. Throughout the paper, we use  $\alpha = 0$  and  $\beta = 0.00008$  for comparisons of loss values.

641 **C COCO Dataset**

642 For the COCO task (Section 5.2), we used subset of images from the MS-COCO dataset [54]. MS-  
 643 COCO was chosen due to its selection of common household objects relevant to the daily life of  
 644 prosthesis users, as well as availability of ground-truth segmentation masks. To select the images  
 645 suitable for prosthetic vision, we filtered out images according to the following criteria:

- 646 1. **Too cluttered.** Any image with greater than 15 total objects was removed. Removed: 15566
- 647 2. **Select chosen objects.** Any image that did not have at least 1 object from the selected categories  
 648 that was larger than 4% of the total image was removed. Removed: 42289
- 649 3. **Too many.** Any image with greater than 5 objects meeting criteria 2 was removed. Removed:  
 650 1017
- 651 4. **Too dim.** Any objects in the image with average pixel brightness less than 50 were discarded. If  
 652 this resulted in an image having 0 remaining objects, the image was removed. Removed: 434

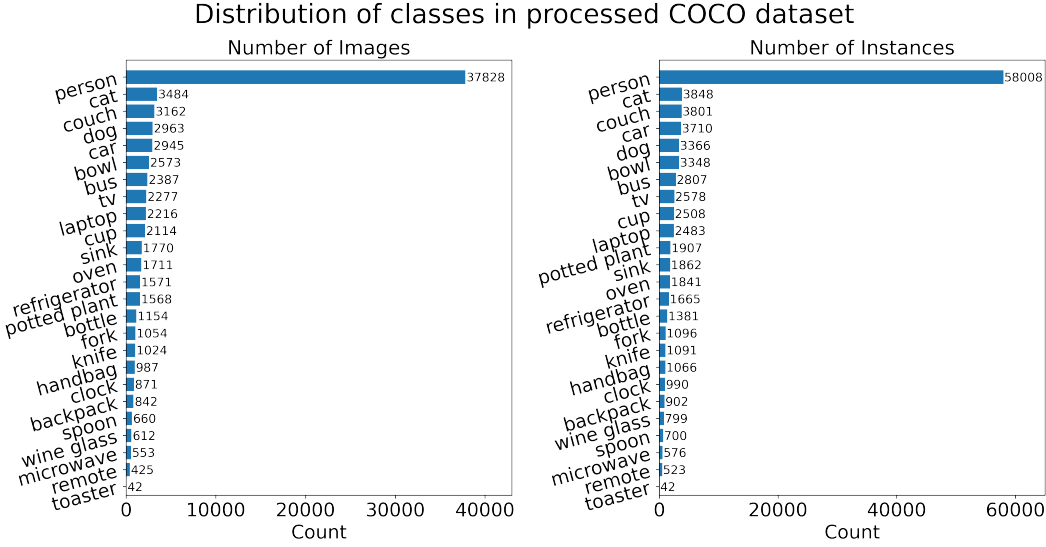


Figure C.1: Number of images (*left*) or instances (*right*) of each category in the processed COCO dataset.

653 This resulted in a total of 47,532 training images and 11,883 test images (80-20 train-test split). The  
 654 objects in the remaining images were segmented out using the ground-truth segmentation masks,  
 655 resized to (49, 49), and converted to grayscale. The distributions of classes used is shown in Figure  
 656 C.1.

657 **D Predicted Stimuli**

658 Here, we directly examine the stimuli resulting from HNA and naive encoders. Stimuli and their  
 659 resulting phosphenes for example images from the test set are shown in Figure D.1. The naive encoder  
 660 produces stimuli with constant frequency (20 Hz) and pulse duration (0.45 ms), which are not shown.

661 We make the following observations about the predicted stimuli:

- 662 • Both encoders activate electrodes corresponding to the shape of the target image. In naive stimuli,  
 663 the amplitude directly corresponds to the pixel brightness. In HNA stimuli, the distributions of  
 664 amplitude, frequency, and pulse duration across the electrodes is more complex and harder to  
 665 characterize, but lead to higher-quality phosphenes.
- 666 • HNA uses amplitudes inversely proportional to  $\rho$ .
- 667 • For small  $\rho$ , HNA primarily uses amplitude to control brightness. For large  $\rho$ , HNA primarily  
 668 uses frequency to modulate brightness, keeping amplitudes low to limit phosphene size.
- 669 • HNA uses small pulse durations to create lines parallel to the underlying axon NFB (*i.e.*, it  
 670 utilizes the streaked phosphenes to its advantage), and large pulse durations to create lines  
 671 perpendicular to the underlying NFB. In other words, HNA was able to exploit application-  
 672 specific (*i.e.*, neuroanatomical) information that is baked into the forward model.
- 673 • On average, HNA uses more electrodes, larger frequencies and pulse durations, and smaller  
 674 amplitudes than the naive encoder. A large active electrode count and high pulse durations may  
 675 not be desirable for some prostheses, due to tissue activation and frame rate limits. We found  
 676 that it was easy to constrain these parameters using regularization on the output stimuli, at the  
 677 cost of slightly decreased performance.

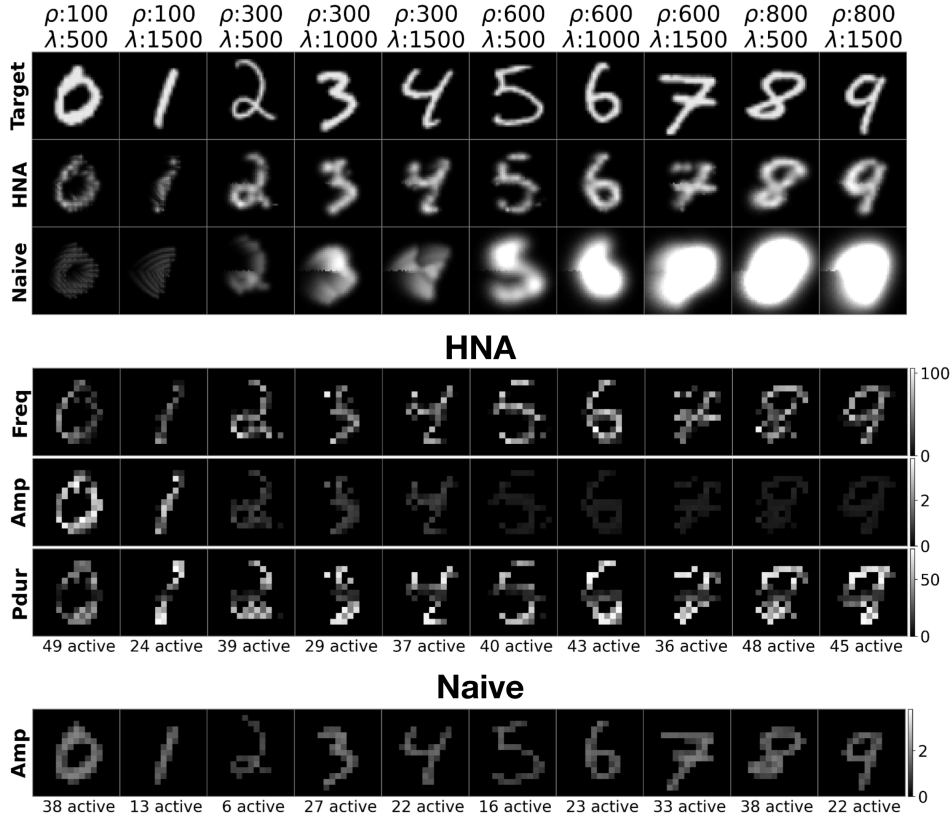


Figure D.1: *Top*: Example MNIST target images, and the phosphenes produced by HNA and naive encoders, encoded at various  $\rho$  and  $\lambda$  values. *Center*: The stimuli corresponding to the HNA phosphenes. From top to bottom, stimulus frequency (Hz), amplitude (xTh), and pulse duration (ms) are shown. The number of 'active' electrodes stimulated above threshold levels is given below each stimuli. *Bottom*: Stimuli corresponding to the naive phosphenes.

## 678 E COCO Patient-to-Patient Variations

679 We repeated the analysis presented in Section 5.3 for the COCO dataset. Figure E.1A shows two  
 680 example COCO images, encoded by both HNA and the naive encoder, across varying  $\rho$  and  $\lambda$   
 681 values. The heatmaps in Figure E.1B show the log of the joint perceptual loss across simulated  
 682 patients, for both the naive and HNA encoders. To measure phosphene consistency, we performed  
 683 T-SNE clustering on a subset of the COCO images which have only 1 object. Unfortunately, T-SNE  
 684 clustering of the ground-truth COCO images did not form groups corresponding to the object types  
 685 (Figure E.1C), suggesting that the representation of object instances vary drastically across COCO  
 686 images. Therefore, it was not meaningful to repeat the analysis presented in Fig. 5C.

687 Similar to the MNIST results presented in Section 5.3, HNA produced higher-quality representations  
 688 than the naive encoder, resulting in a lower joint loss for every simulated patient. HNA performed  
 689 consistently well across all simulated patients (Figure E.1B), with a small increase in loss for small  $\rho$   
 690 ( $< 100$ ). Similar to MNIST, the naive encoder only performs well for patients with a mid-to-low  $\rho$   
 691 ( $\approx 200$ ) and low  $\lambda$ .

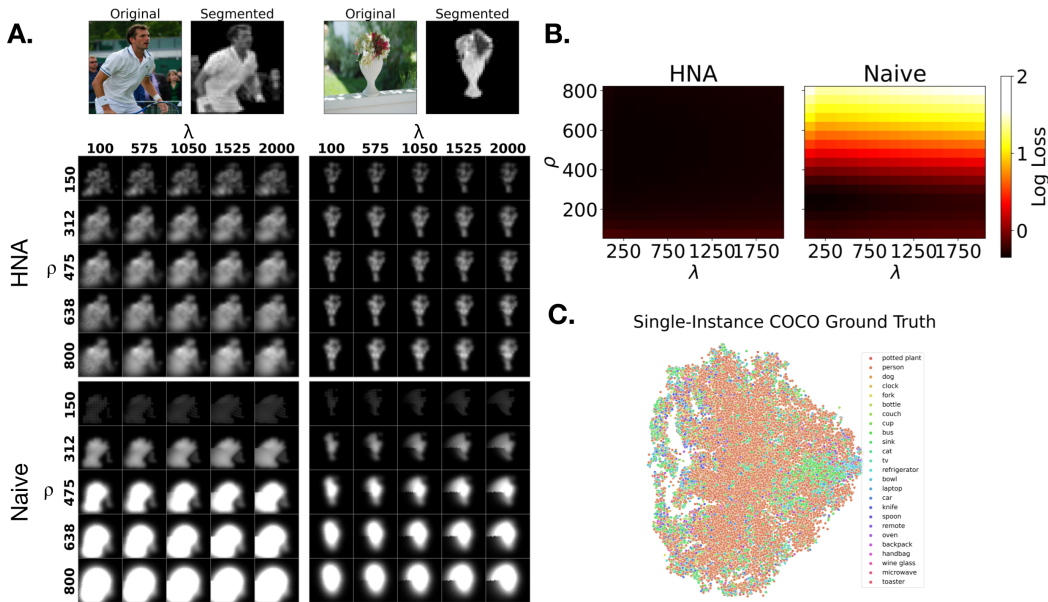


Figure E.1: COCO Encoder performance across simulated patients (varying  $\rho$  and  $\lambda$ ). **A:** Phosphenes produced by HNA and Naive encoders of two example images. **B:** Heatmaps showing the log joint loss across  $\rho$  and  $\lambda$  for HNA and naive encoders. **C:** Ground-truth COCO images cannot be clustered using T-SNE into groups corresponding to the object types. The clustering was performed on COCO images that only contained one object.

## 692 F Modeling Other Patient-to-Patient Variations

693 Previously, results were presented across patient-specific parameters  $\rho$  and  $\lambda$ , because these have  
 694 the greatest impact on phosphene appearance. However, the forward model has a number of other  
 695 patient-specific parameters, which HNA is also able to adapt to. For full details on all parameters of  
 696 the forward model, see [23]. Out of the remaining parameters,  $a_2$ ,  $a_3$ , and  $a_5$  are the most impactful  
 697 on phosphene appearance.  $a_2$  and  $a_3$  modulate how much the brightness contribution from each  
 698 electrode scales with increasing amplitude and frequency, respectively.  $a_5$  locally scales the global  
 699 radial current spread  $\rho$  based on each electrodes amplitude. Figure F.1 (*left*) illustrates the effect of  
 700 these parameters on phosphene appearance.

701 Figure F.1 compares HNA to naive encoder performance across  $a_2$ ,  $a_3$ , and  $a_5$ . The ranges for these  
 702 parameters are based on values empirically observed in retinal prosthesis users [23]. HNA produces  
 703 relatively consistent phosphenes, and outperforms the naive encoder across all conditions.

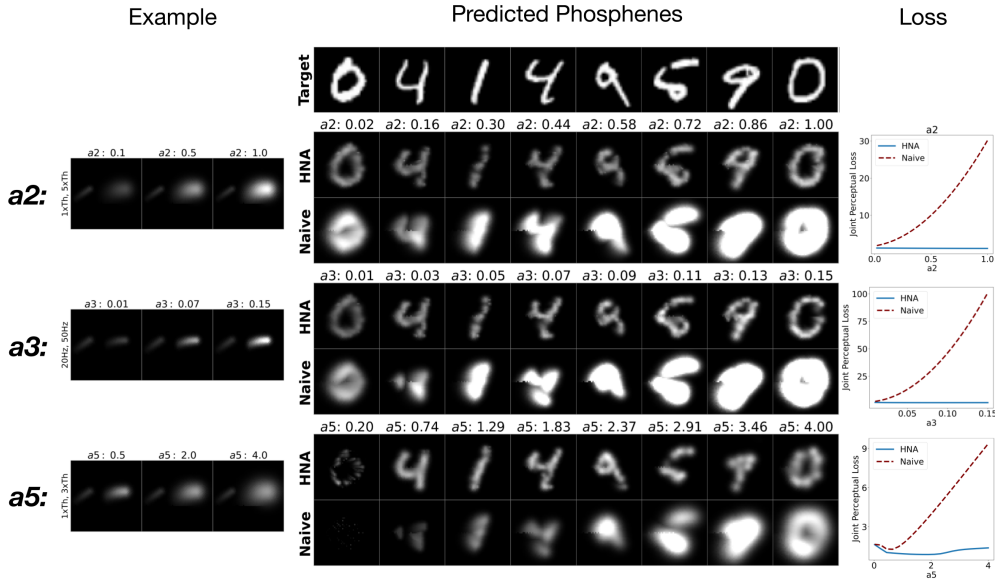


Figure F.1: *Left:* Examples of how  $a_2$ ,  $a_3$ , and  $a_5$  affect single-electrode phosphenes.  $a_2$  modulates local brightness scaling with increasing amplitude,  $a_3$  modulates local brightness scaling with increasing frequency, and  $a_5$  modulates local size scaling with increasing amplitude. *Center:* Phosphenes predicted with HNA and naive encoders for varying  $a_2$ ,  $a_3$ , and  $a_5$ , increasing left to right. *Right:* Plot showing the joint loss across  $a_2$ ,  $a_3$ , and  $a_5$  for HNA (solid) and naive encoder (dashed line).

704 **G Simulating Higher-Resolution Implants**

- 705 On the COCO task, HNA significantly outperformed the naive encoder, but was still unable to capture  
 706 all of the detail in the images. Two of the main reasons for this are the limited spatial resolution of the  
 707 implant and the patient-specific distortions from the forward model. Here, we present results from  
 708 HNAs trained on implants of higher resolution, at small  $\rho$  and  $\lambda$ . The chosen implants are illustrated  
 709 in Figure G.1A. For a fair comparison, each HNA was trained for only 50 epochs.
- 710 Phosphenes resulting from the HNA trained on the different implants are shown in Figure G.1C, and  
 711 the losses across implants is plotted in Figure G.1B. As implant resolution increases, the phosphenes  
 712 look increasingly similar to the ground truth, and small details (e.g. facial details, textures) start to  
 713 emerge.
- 714 Thus, HNAs initial failure to capture high-frequency details in the image appears to be an application-  
 715 specific limitation for visual prostheses more so than a limitation of the HNA framework. For visual  
 716 prostheses, learning to reconstruct the high-frequency features of complex images despite distortions  
 717 and limited implant resolution remains an open problem.

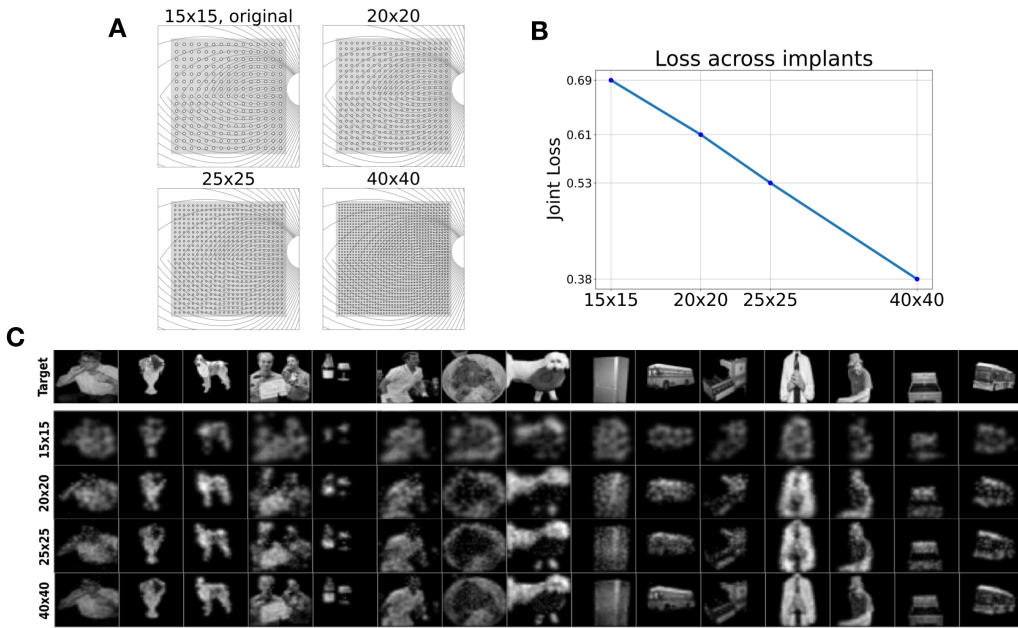


Figure G.1: **A:** The 4 different implants compared. The main text uses the  $15 \times 15$  implant. **B:** The joint perceptual loss of HNAs trained on the different implants after 50 epochs. **C:** Example images showing the reconstructed phosphenes using each implant

718 **H Mis-Specified Patient-Specific Parameters**

719 Due to noisy or limited patient data, there may be some uncertainty in the measured value of the  
 720 patient-specific parameters  $\phi$ . Therefore, we conducted an analysis of the consequences of incorrect  
 721 patient-specific parameters on the encodings produced by HNA. Note that the true patient-specific  
 722 parameters are not needed during training, so incorrect  $\phi$  will only affect evaluation. A 'mismatch'  
 723 HNA model was created, where the forward model decoder used the true patient-specific parameters  
 724  $\phi$ , and the encoder used another set of patient-specific parameters  $\phi'$ .

725 In the first experiment,  $\phi'$  was sampled from a uniform random distribution (we again focus on only  $\rho$   
 726 and  $\lambda$ ). The original HNA encoder, naive encoder, and mismatch HNA encoder with random  $\phi'$  were  
 727 evaluated on the MNIST test set. HNA achieved a joint loss of 0.92, the naive encoder had a joint  
 728 loss of 3.13, and the mismatch HNA had a joint loss of  $1.35 \pm 0.003$  (mean  $\pm$  standard deviation  
 729 across 10 random  $\phi'$ ). Thus, even if the true patient-specific parameters are completely unknown, on  
 730 average randomly selecting values will still produce higher-quality encodings than the naive method.

731 In a second experiment, we analyzed whether there were any configurations ( $\phi - \phi'$  combinations)  
 732 that resulted in a worse encoding than the naive model. For the 90% of true  $\phi$ , the mismatch model  
 733 outperformed the naive model regardless of the chosen  $\phi'$ . However, the naive model performs best at  
 734  $\rho = 250$  and  $\lambda = 200$ . In Figure H.1A, we hold  $\lambda$  constant at 200 and, for each true  $\rho$ , plot the ranges  
 735 of mis-specified  $\rho'$  for which the mismatch HNA still outperforms the naive. Figure H.1B shows a  
 736 similar plot for varying  $\lambda$ , holding  $\rho$  constant at 250. Even for the naive model's ideal patients, HNA  
 737 still outperforms the naive model for a large proportion of mis-specified  $\rho$  and  $\lambda$ .

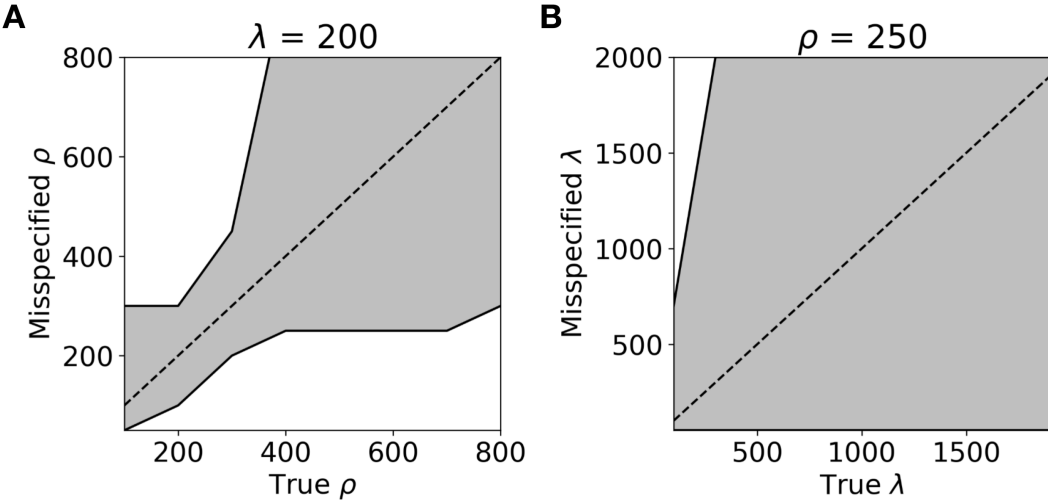


Figure H.1: Plots showing mis-specified HNA performance relative to the naive encoder for varying  $\rho$  (panel A) and  $\lambda$  (panel B). The dashed line marks the correctly specified model, and shaded area between the solid lines shows the region where the mis-specified HNA outperforms the naive encoder. Note that the naive model's ideal patient was used, with  $\lambda$  fixed at 200 and  $\rho$  fixed at 250, respectively.